

SPACECRAFT TRAJECTORY TRACKING AND PARAMETER ESTIMATION AROUND A SPLITTING CONTACT BINARY ASTEROID

Tiago M. Silva^{*}, Jean-Baptiste Bouvier[†], Kathleen Xu[‡],
Masatoshi Hirabayashi[§], and Koki Ho^{**}

Increasing interest in asteroid mining and in-situ resource utilization will lead to an increase in asteroid surface operations. The geophysical properties of asteroids are often unknown and play a significant role in the resulting gravitational fields. Surface operations such as mining may significantly alter the asteroid's structure or, in the case of contact binary asteroids, cause the asteroid to split depending on the rotational condition. The coupled problem of estimating unknown parameters of a splitting contact-binary system and controlling a spacecraft's trajectory in the system's vicinity is investigated. An indirect adaptive control scheme is utilized to simultaneously meet both objectives. The results are compared with the traditional 2-body controller and the improvement enabled by the proposed scheme is demonstrated.

INTRODUCTION

A greater emphasis on asteroid exploration missions has arisen in the last few decades. Missions include collecting asteroid material for the purposes of scientific study and engineering advancement. Hayabusa, an asteroid sample return mission led by the Japan Aerospace Exploration Agency (JAXA), explored the asteroid Itokawa¹. The mission was partially successful with many engineering issues, and the spacecraft eventually recovered a limited amount of a surface material sample of the asteroid and brought it back to Earth². JAXA-led Hayabusa2^{3,4,5} and NASA-led OSIRIS-REx^{6,7} are currently attempting to sample materials from the asteroids (162183) Ryugu and (101955) Bennu, respectively. To sample materials, the Hayabusa2 mission landed on Ryugu's surface, sent a high-speed projectile to the surface, and collected fragmented materials in its sampling chambers². In addition, the OSIRIS-REx mission will attempt to collect materials by exerting gas pressure onto the asteroid surface, stirring material up into the sampling system⁷.

Small sample return missions are merely a subset of the expanding number of those requiring asteroid surface operations. Future mission concepts sometimes include plans for direct interactions of spacecraft with surface materials⁸ and the structure of asteroids due to controlled explosions⁹. Interest regarding the economic potential of asteroid missions is growing as countries such as the US and Luxembourg develop a legal framework for the industry^{10,11}. Finally, deflecting or redirecting potential hazardous asteroids provides another practical application requiring surface operations. NASA's Double Asteroid Redirect Test (DART) is an ongoing mission to impact a smaller, secondary component of (65803) Didymos, a binary Near Earth Asteroid (NEA). Part of the DART mission involves releasing a CubeSat before the impact, making the kinetic deflection capability an important consideration for the mission^{12,13,14}.

^{*} Formerly M.S. Student, Aerospace Engineering, University of Illinois at Urbana-Champaign, 104 South Wright Street, Urbana, IL 61801

[†] PhD Student, Aerospace Engineering, University of Illinois at Urbana-Champaign, 104 South Wright Street, Urbana, IL 61801

[‡] Undergraduate Student, Aerospace Engineering, University of Illinois at Urbana-Champaign, 104 South Wright Street, Urbana, IL 61801

[§] Assistant Professor, Aerospace Engineering, Auburn University, 211 Davis Hall, Auburn, AL 36849.

^{**} Assistant Professor, Aerospace Engineering, Georgia Institute of Technology, North Avenue NW, Atlanta, GA, 30332.

The geophysical properties of asteroids must be considered when discussing asteroid missions, regardless of the mission's purpose. Different asteroid compositions, sizes, and shapes lead to different scientific objectives and engineering considerations. The geophysical properties play an important role; many small asteroids may be gravitational aggregates of regolith and boulders, or so-called rubble piles as inferred from observations of the asteroids¹⁵. Itokawa was measured to have a bulk density of 1.9 g/cm³, and a unique shape and surface morphology². Such asteroids do not have great mechanical strength, which is reportedly about 100 Pa^{15,16}, implying that they occasionally experience local and global landslides and internal deformation processes. These processes have been proposed to result from fast rotation, hypervelocity micrometeorite impacts, and tidal effects. The shape is a critical asteroid feature affecting the potential deformation modes for the asteroid¹⁶. Asteroids are categorized into four critical shapes: spheroidal, elongated, contact-binary, and non-classified shapes¹⁷. As mentioned above, some asteroids have relatively fast rotation rates, which cause higher sensitivity to structural deformation as centrifugal forces become dominant. With such weak cohesive forces and higher centrifugal forces, structural failure can occur. The main belt asteroid P/2013 R3 has been observed breaking into multiple distinct parts, thought to be caused by structural failure¹⁸.

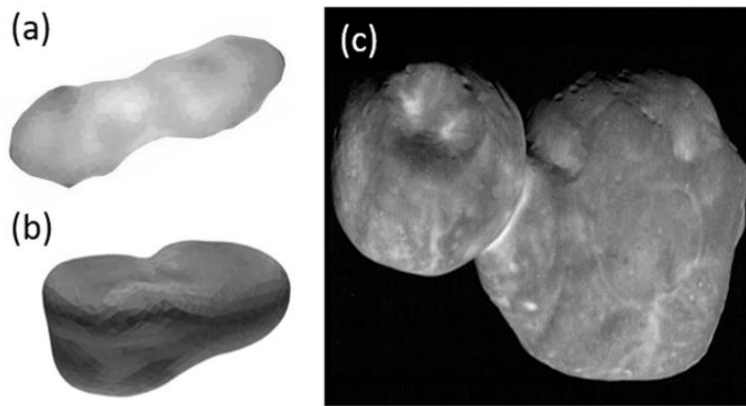


Figure 1. Contact-binary examples: (a) the shape of Kleopatra¹⁹, (b) the shape of Castalia²⁰, (c) the image of 2014 MU₆₉²¹.

A contact-binary asteroid is an asteroid that consists of two large lobes resting on each other. Contact binaries may be formed by a gentle merger of two similar-sized components resulting in a potentially weakly bound single body²². Recent observations have shown that contact-binary configurations are common in the solar system. Ground observations have shown that up to 10-20% of observed asteroids exhibit features of contact binaries¹⁷. For example, Itokawa is classified as a contact-binary². Other examples of contact binaries include Castalia and Toutatis in the NEAs, Kleopatra in the main belt asteroids, and the icy body 2014 MU₆₉ in the Kuiper belt^{23,24}. For cometary nuclei, observations have revealed that up to 70% of the observed objects at high resolution are contact binaries. For instance, the comet 67P/Churyumov-Gerasimenko has a contact-binary nucleus²⁵.

Spacecraft trajectory control about asteroids is a topic of frequent study. Asteroid geophysical properties are difficult to estimate, so acknowledging model uncertainties and/or unknown parameters is needed in analysis; however, commonly used models assume knowledge of parameters such as the moment of inertia and density. While these models give useful insight into leveraging the natural dynamics about asteroid systems^{26,27,28}, the online model refinement accounting for model uncertainties and/or unknown quantities is absent. Asteroid deformation and its effect on the gravity field has also been visited in the literature^{16,29,30}. However, spacecraft control in light of unknown system parameters which characterize the process of an asteroid's deformation has not been addressed in the literature.

In this work, a hypothetical situation is considered in which a spacecraft is near a contact-binary asteroid that undergoes deformation. Structural instability (either natural or induced by surface operations) causes the two lobes of the asteroid to split. A simple model is introduced in which a contact-binary is assumed to comprise of two lobes, each with a point-mass gravitational field assumption. The contributions of this work are threefold. First, conditions for a bounded, splitting contact-binary system were derived. Second, an observable set of parameters that characterize the splitting contact-binary system was identified. Third, a control and estimation technique for robustly achieving the desired trajectory and estimating the split-characterization parameters after the two elements are no longer in contact was developed. Finally, the importance of including the splitting characterization in the controller is analyzed and demonstrated. Simulations have characterized the performance increase of using the proposed adaptive controller over a more traditional control approach.

A few remarks need to be made about the assumptions in this work. The gravitational model for the problem affects the evolution of the separated contact-binary system as well as the trajectory of the spacecraft in orbit. There are several common methods for modeling gravitational fields for irregularly shaped bodies. The most common is the spherical harmonic method where the gravitational potential of a body is represented as a sum of spherical harmonics (e.g. the J_2 perturbation in Earth orbit is the dominating perturbing harmonic)³¹. Alternatively, ellipsoidal and polyhedral shape models have been used previously for this purpose^{32,33}. Accurately using any of these models for a particular asteroid requires knowledge of the asteroid's density, which is likely non-uniform and would require significantly more computation time than the point-mass gravitational field to simulate. Since the filtering method accounts for perturbations to the process, the model used for this work can be used to demonstrate accurate control in light of deviations from the simple gravity model. The point-mass field assumption is used to save on computation time while having the capability to accurately estimate the current state of the spacecraft. Since the problem of controlling a spacecraft's trajectory about a separated contact-binary system has not yet been addressed in the literature, using the point-mass assumption for analysis allows conclusions to be drawn about the feasibility of the control method without requiring extensive computation time. Detailed gravitational models can be used to extend this work and verify the applicability of the method to particular asteroids.

METHODOLOGY

Modeling

A model is needed to govern the evolution of a splitting contact-binary system that consists of two lobes with masses of m_1 and m_2 . The 2-body problem is used for the asteroid system model, using the point mass gravitational field assumption. To get the equation of motion (EOM) for the separation distance, the centrifugal force and the gravitational forces on the asteroid are balanced:

$$\ddot{d} = \Omega^2 d - \frac{G(m_1 + m_2)}{d^2} \quad (1)$$

This describes the dynamics in the frame rotating with the asteroid system as a differential equation for the separation distance between two asteroid lobes, d . Using conservation of angular momentum, the angular velocity, Ω , can be rewritten as a function of the separation distance:

$$\Omega = \Omega_0 \frac{I_n + \mu(1 - \mu)d_0^2}{I_n + \mu(1 - \mu)d^2} = \frac{L_{n0}}{I_n + \mu(1 - \mu)d^2} \quad (2)$$

Finally, the EOM for the separation distance in Equation (3) is an ordinary differential equation (ODE):

$$\ddot{d} = \Omega_0^2 d \left(\frac{I_n + \mu(1 - \mu)d_0^2}{I_n + \mu(1 - \mu)d^2} \right)^2 - \frac{Gm_{tot}}{d^2} \quad (3)$$

Ω_0 is the initial angular velocity of the system, d_0 is the initial splitting distance of the asteroid lobes, I_n is the sum of the moments of inertia of both asteroid lobes divided by the total mass, L_{n0} is the initial angular momentum of the asteroid system divided by the total mass, μ is the ratio of the second mass to the total mass, and G is the gravitational constant*. Conservation of energy was used to analyze the different modes for the system. In total there are three: the asteroid splits, but do not have enough kinetic energy to separate (Case I); the asteroid splits, have enough energy to separate, but remain in a bounded orbit about each other (Case II); the asteroid splits, have enough energy to separate, and achieve an escape trajectory from each other (Case III). Conditions on the system parameters for the three regimes are given next†:

* For definitions for all notation (symbols and acronyms) used in the text, refer to the Notation section before the Appendices.

† Derivations of these bounds can be found in Appendix A.

$$\begin{aligned}
\text{(I)} \quad & 0 \leq \Omega_0^2 \leq \frac{Gm_{tot}}{d_0^3} \\
\text{(II)} \quad & \frac{Gm_{tot}}{d_0^3} < \Omega_0^2 < \frac{Gm_{tot}}{d_0} \cdot \frac{2\mu(1-\mu)}{I_n + \mu(1-\mu)d_0^2} \\
\text{(III)} \quad & \frac{Gm_{tot}}{d_0} \cdot \frac{2\mu(1-\mu)}{I_n + \mu(1-\mu)d_0^2} \leq \Omega_0^2 < \infty
\end{aligned} \tag{4}$$

The three cases are illustrated in the figure below in Figure 2. The equilibrium separation distance is given as the dotted line in the plots. This distance can be solved analytically by solving a quartic equation resulting from setting time derivative terms in the EOMs to zero and solving for the distance. Notice that Case II gives oscillation about the equilibrium point. For the work done here, only Case II is desirable since Case I is the same as the case before splitting and Case III limits the duration of usefulness for maintaining an orbit about the binary system.

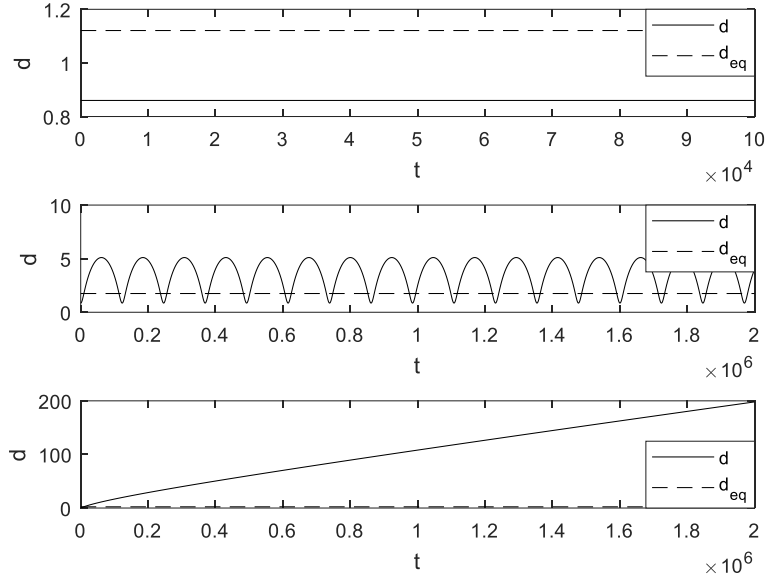


Figure 2. Top to bottom: cases I, II, and III for the dynamic evolution of the binary system. The separation distance is given in km, time is given in seconds. These parameters are given in Table 1.

A spacecraft near the asteroid system is assumed to have negligible mass, so in the rotating frame of the asteroid lobes, the 3-body problem can be used to govern the motion of the spacecraft. For control design, it is necessary to represent the EOM for the 3-body problem in a general, inertial frame. To do this, an XYZ Euler angle sequence is used with three Euler angles γ_1 , γ_2 , and θ . The angles γ_1 and γ_2 are assumed to be fixed, merely to change the plane in which the asteroid rotates (frame 3) with respect to some general inertial frame (frame 0) in which the spacecraft takes measurements and applies control. The position of the spacecraft with respect to the asteroid is shown in Figure 3 prior to the asteroid's separation. Figure 4 shows the relative position of the spacecraft with respect to the split components at a later time, after separation. In this figure, the inertial and rotating frames are misaligned. They are related through the Euler angle sequence, which has the associated rotation matrix, R_3^0 . d is a function of time, based on the 2-body dynamics of the asteroid.

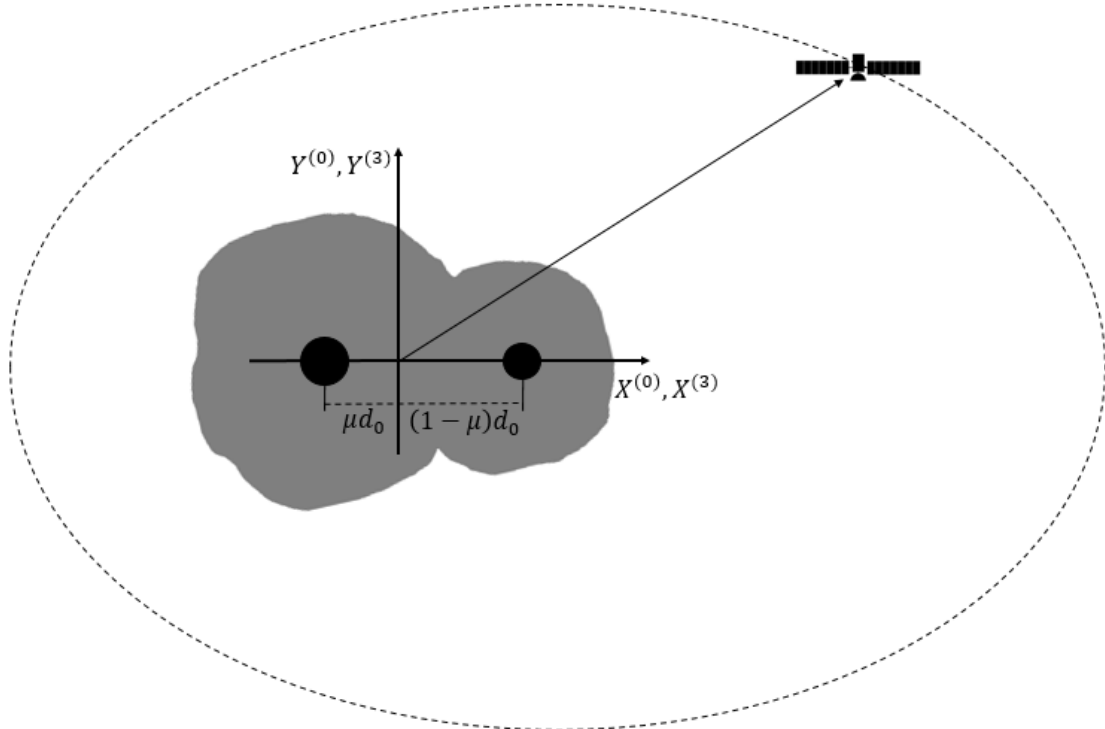


Figure 3. Point-mass gravitational field model for contact-binary asteroid prior to separation. Two aligned frames are shown, the inertial frame (frame 0) and the rotating frame (frame 3).

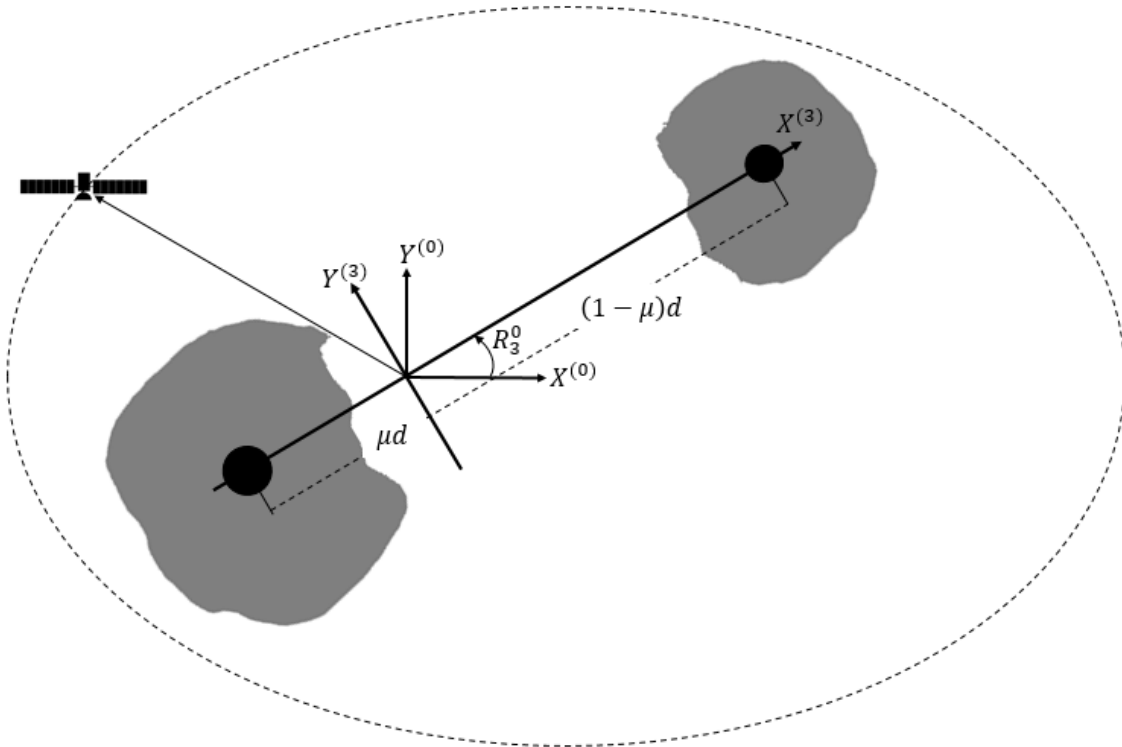


Figure 4. Point-mass gravitational field model for a contact-binary asteroid after separation. Inertial and rotating frames are related via an XYZ Euler angle sequence with a rotation matrix R_3^0 , parameterized by the angles $(\gamma_1, \gamma_2, \theta)$.

The well-known EOMs in the rotating frame for the 3-body problem are given here. It's important to realize that using the Euler angle sequence given, the angle θ has a time derivative Ω , the angular velocity of the asteroid system. The EOMs are:

$$\ddot{x}^{(3)} = 2\Omega\dot{y}^{(3)} + \Omega^2x^{(3)} + y^{(3)}\dot{\Omega} - \frac{Gm_1(x^{(3)} + \mu d)}{r_1^3} - \frac{Gm_2(x^{(3)} - (1 - \mu)d)}{r_2^3} + \frac{u_1^{(3)}}{m_{sc}} \quad (5)$$

$$\ddot{y}^{(3)} = -2\Omega\dot{x}^{(3)} + \Omega^2y^{(3)} - x^{(3)}\dot{\Omega} - \frac{Gm_1y^{(3)}}{r_1^3} - \frac{Gm_2y^{(3)}}{r_2^3} + \frac{u_2^{(3)}}{m_{sc}} \quad (6)$$

$$\ddot{z}^{(3)} = -\frac{Gm_1z^{(3)}}{r_1^3} - \frac{Gm_2z^{(3)}}{r_2^3} + \frac{u_3^{(3)}}{m_{sc}} \quad (7)$$

Superscripts denote each variable's frame of reference per the convention illustrated in Figure 3 and Figure 4 – frame 0 is the inertial frame and frame 3 is the rotating frame. Control appears as the input u with (x, y, z) components u_1 , u_2 , and u_3 , respectively. For implementation, control is applied in the inertial frame, however, it is represented in the rotating frame for brevity. Inputs are bounded by the thruster capabilities of the spacecraft. The equations for the angular acceleration of the rotating frame is the time derivative of Ω in Equation (2):

$$\dot{\Omega} = \frac{\partial \Omega}{\partial d} \dot{d} = \left(-2\mu d(1 - \mu) \frac{L_{n0}}{(I_n + \mu(1 - \mu)d^2)^2} \right) \dot{d} \quad (8)$$

Estimation and Adaptive Control

Now that the system model is established, unknown parameters in the system must be identified. The model for the system includes constant parameters which cannot be taken to be known. The mass distribution of each asteroid lobe, the moment of inertia of each asteroid lobe, the initial angular momentum of the asteroid lobes, and the plane of rotation of the asteroid lobes are all unknown immediately after the split. Therefore, to develop a control method, techniques from the field of adaptive control can be used. Direct methods for adaptive control combine the control objective and the parameter estimation in one step, whereas the indirect methods used here separate the parameter estimation and the control into two steps³⁴. Direct methods generally rely on developing forms for the parameter estimators unique to the problem, such that the estimation error and the trajectory error are driven to zero simultaneously. Often, Lyapunov functions are used to facilitate these direct adaptive control methods. No closed-form Lyapunov function is known for our problem and finding a suitable function to that end is beyond the scope of this work. The indirect control method is chosen as it sufficiently meets both objectives: trajectory tracking and parameter estimation.

The indirect method used for parameter estimation is a dual method for state and parameter estimation. A Kalman filter or its variant is used to convert noisy observations of the system process (also noisy) into state and parameter estimates used for the controller. This method for simultaneous state and parameter estimation is quite common^{35,36,37}. The state used in the Kalman filter is an extended state containing the dynamic variables (state variables) and the set of unknown parameters. By this logic, the parameter estimation and control method are separated and the control is based on the Certainty Equivalence Principle (CEP). This just means that the parameter estimates are taken to be true for the purposes of determining the appropriate control³⁴. The extended state for our problem is given below. Variables are given in inertial coordinates where appropriate (L_{n0} is the initial angular momentum of the system divided by the total mass):

$$X := [x^{(0)}, y^{(0)}, z^{(0)}, d, \dot{x}^{(0)}, \dot{y}^{(0)}, \dot{z}^{(0)}, \dot{d}, \theta, \mu, L_{n0}, I_n, \gamma_1, \gamma_2]^T \quad (9)$$

Observability. The parameter estimation method depends on the system being observable since the Kalman filter relies on an observable system to convert the noisy observation into extended state estimates³⁶. For linear systems, observability can be checked using a rank condition of the observability matrix. A similar rank condition is required for nonlinear systems, however, the matrix is a function of the state and the condition must be true for any

value of the state³⁸. The matrix is made up of successive Lie derivatives of the observation with respect to the flow of the system. These Lie derivative fields are concatenated into a vector, then the Jacobian of that vector with respect to the extended state of the system gives the nonlinear version of the observability matrix. Consider the system given below, where ξ is the state and η is the measurement:

$$\begin{aligned}\dot{\xi} &= f_{\xi}(\xi), \quad \xi \in \mathbb{R}^n \\ \eta &= h_{\xi}(\xi), \quad \eta \in \mathbb{R}^m\end{aligned}\tag{10}$$

The observation is achieved through the mapping h_{ξ} . The flow of the system is given by the field f_{ξ} for the state ξ . Now, the successive Lie derivatives are:

$$\begin{aligned}L_f \phi_i &= \frac{\partial \phi_i}{\partial \xi} f_{\xi}(\xi) \\ \phi_0 &= h_{\xi}(\xi) \\ \phi_i &= L_f \phi_{i-1}, \quad i = 1, \dots, n-1\end{aligned}\tag{11}$$

The zeroth order Lie derivative is taken to be the observation mapping. In the subsequent sections, the ratio $\partial w / \partial v$ or symbol $\partial_v w$ of two vectors $w \in \mathbb{R}^q$ and $v \in \mathbb{R}^p$ both represent the $q \times p$ Jacobian matrix.

Next, the Lie derivatives must be concatenated into a single vector given by Φ . This vector and the (local weak) observability rank condition for the state-dependent observability matrix $\partial_{\xi} \Phi$ for nonlinear systems is:

$$\begin{aligned}\Phi &= [\phi_0^T, \phi_1^T, \dots, \phi_{n-1}^T]^T \\ \text{rank} \left\{ \frac{\partial \Phi}{\partial \xi} \right\} &= n\end{aligned}\tag{12}$$

The extended state X discussed before and the observation mapping are used for the present problem where the system is observable by this condition. This was verified analytically using symbolic math software. The observation mapping used for this case is the relative position and velocity of the spacecraft with respect to both asteroids, given in the inertial frame (12 components total). The observation and its Jacobian are important for the estimation process.

Extended Kalman Filter. The Kalman filter used to give state and parameter estimates is the continuous-discrete version of the Extended Kalman Filter (EKF). The continuous discrete filter uses continuous dynamics to give state and error predictions and discrete measurements to update the state predictions and error accordingly. Consider the general dynamical system and observation mapping given by:

$$\begin{aligned}\dot{\xi} &= f_{\xi}(\xi, t) + W(t), \quad \xi \in \mathbb{R}^n \\ \eta &= h_{\xi}(\xi) + V(t), \quad \eta \in \mathbb{R}^m\end{aligned}\tag{13}$$

$W(t)$ and $V(t)$ are additive zero-mean Gaussian Random Vectors (RVs) that represent the process noise and the measurement noise, respectively. The covariance of $W(t)$ is $Q_{EKF} \in \mathbb{R}^{n \times n}$ and the covariance of $V(t)$ is $R_{EKF} \in \mathbb{R}^{m \times m} \forall t$.

The estimation process is split into two parts: prediction and estimation. The prediction step is represented as a set of ODEs for the prediction error matrix ($P_{EKF} \in \mathbb{R}^{n \times n}$) and the state estimate ($\bar{\xi} \in \mathbb{R}^n$). These equations are:

$$\begin{aligned}\dot{\bar{\xi}} &= f_{\xi}(\bar{\xi}, t) \\ \dot{P}_{EKF} &= F_{\xi} P_{EKF} + P_{EKF} F_{\xi}^T + Q_{EKF}, \quad F_{\xi} = \left. \frac{\partial f_{\xi}}{\partial \xi} \right|_{\xi=\bar{\xi}}\end{aligned}\tag{14}$$

If the current time is τ and measurements are received between intervals of length Δt , then the prediction step ODEs must be integrated together on the interval $t \in [\tau, \tau + \Delta t]$. This will give the predicted state and predicted error matrix for the update step: $\bar{\xi}^- = \bar{\xi}(\tau + \Delta t)$ and $P_{EKF}^- = P_{EKF}(\tau + \Delta t)$, respectively.

The update step corrects the prediction error matrix and the predicted state estimate using the most recent discrete-time measurement. These updates are achieved through the algebraic equations:

$$\begin{aligned}
K_{EKF} &= P_{EKF}^- H_{\xi}^T (H_{\xi} P_{EKF}^- H_{\xi}^T + R_{EKF})^{-1}, & H_{\xi} &= \left. \frac{\partial h_{\xi}}{\partial \xi} \right|_{\xi=\bar{\xi}^-} \\
\bar{\xi} &= \bar{\xi}^- + K_{EKF} (\eta - h_{\xi}(\bar{\xi}^-)) \\
P_{EKF} &= (I_{n \times n} - K_{EKF} H_{\xi}) P_{EKF}^- (I_{n \times n} - K_{EKF} H_{\xi})^T + K_{EKF} R_{EKF} K_{EKF}^T
\end{aligned} \tag{15}$$

The prediction-update process is repeated for every measurement, using the updated prediction error matrix and state estimate of the previous step as the initial condition for the ODE in the prediction step each time. The Joseph form of the a posteriori error covariance update is used since K_{EKF} is not guaranteed to be optimal gain for the true nonlinear system, only for the linearized system. This form is more numerically stable and robust than the standard update equation³⁹.

To use the EKF within the indirect adaptive control scheme discussed in this work, the dynamic system for the variable ξ in Equations 13 – 15 is replaced by that for the extended state, X , defined in Equation 9. Since some elements of X are constant parameters, the corresponding elements of the field f_X will be zero. However, the corresponding elements of the process noise covariance matrix must be non-zero and are chosen based on filter stability³⁵.

The Unscented Kalman Filter (UKF), which is cited to give better state estimates for many nonlinear systems⁴⁰, was considered also. Due to the required matrix square root of the algorithm, the UKF increases the computation time and complexity of numerical implementation. The UKF also introduces additional parameters which need to be tuned for the filter's stability. Practically, after implementing both the EKF and UKF, using the observability index as a measure⁴¹, the UKF either provided little advantage or worse performance when applied to this problem. Additional steps in the UKF, such as the Cholesky factorization used for taking the matrix square root may accrue errors not seen in the EKF, causing the EKF to perform better in practice.

For estimation, a few assumptions about the noise and measurements are made. Gaussian noise is assumed for the process noise and the measurement noise using covariance matrices to generate the RVs for each. The spacecraft is assumed to possess the required sensors and/or information to obtain noisy measures of its relative distance and velocity with respect to each lobe of the asteroid in the inertial frame.

Control Design. The control objective considered here is trajectory tracking. The goal is to match both the position and velocity of some reference or desired trajectory. The desired state is denoted as X_d and is made up of the desired position and velocity of the spacecraft. Our desired trajectory is chosen to be a Keplerian elliptic orbit about the asteroid system. This trajectory can be generated as a function of time using the f and g functions presented in Reference 42. In general, the trajectory can be of any form as long as the position and velocity for each time can be obtained. The control method used here is a nonlinear version of an LQR controller based on the formulation used for trajectory tracking⁴³. The estimated state X_t contains only the dynamic variables in X related to position and velocity: x , y , z , \dot{x} , \dot{y} , and \dot{z} . The state X_t is governed by the EOMs in Equations (5 – 8). First, the trajectory tracking problem is converted into a stabilization problem via a change of coordinates into an error state based on the spacecraft's trajectory and the desired trajectory. After changing coordinates, the EOMs for the error system are linearized using a first order Taylor series expansion about zero-error. This is done in order to get the nonlinear system to take the form of a linear time varying system that is used to formulate the LQR controller for some control input u . Since the adaptive control method is indirect, X_t is the estimated state (position and velocity only) applied to this problem, which is obtained using the EKF on the extended state X in the previous subsection. The error state and linearized error system are given by:

$$e = X_t - X_d \tag{16}$$

$$\dot{e} = A_e(t)e + B_e u, \quad A_e(t) = \left. \frac{\partial f_e}{\partial e} \right|_{e=0}$$

Now the control is obtained by solving the differential Riccati equation (DRE) backward in time each time a new control is required (i.e. each time the integrator for the EOMs requires a time step). Quadratic cost is minimized in both the error state and the control input. This cost depends on weights Q , R , N , and F . The cost is given by:

$$J = e^T(t_f)F e(t_f) + \int_{t_0}^{t_f} (e^T Q e + u^T R u + 2e^T N u) d\tau \quad (17)$$

The DRE and its final condition are given by:

$$\begin{aligned} -\dot{P} &= P A_e + A_e^T P - (P B_e + N) R^{-1} (B_e^T P + N^T) + Q \\ P(t_f) &= F \end{aligned} \quad (18)$$

Finally, the LQR time-dependent feedback control is given by:

$$\begin{aligned} u(e, t) &= -K(t)e \\ K(t) &= R^{-1} (B_e^T P(t) + N^T) \end{aligned} \quad (19)$$

This model assumes the controller to be inherently unbounded. However, the control may be saturated at the physical limitations of the thrusters or, using a more rigorous approach. To address this issue, it can be bounded using eigenvalue placement⁴⁴. The former has been implemented in simulations and works well as long as the control input is on the same order as the 3-body perturbations.

CASE STUDIES

Control Cases

This section highlights the importance of using the proposed adaptive controller to track the trajectory over other methods. If the spacecraft experiences only 2-body dynamics, then it would follow a Keplerian trajectory regardless. However, when 3-body effects and process noise are added to the dynamics, this is no longer the case. Figure 5 shows that with no control, the spacecraft rapidly deviates from the ~9 km semi-major axis Keplerian trajectory in the 3-body problem. Asteroid Castalia, which is modeled to be a system that two masses are connected by a constant bar, was used for this example.

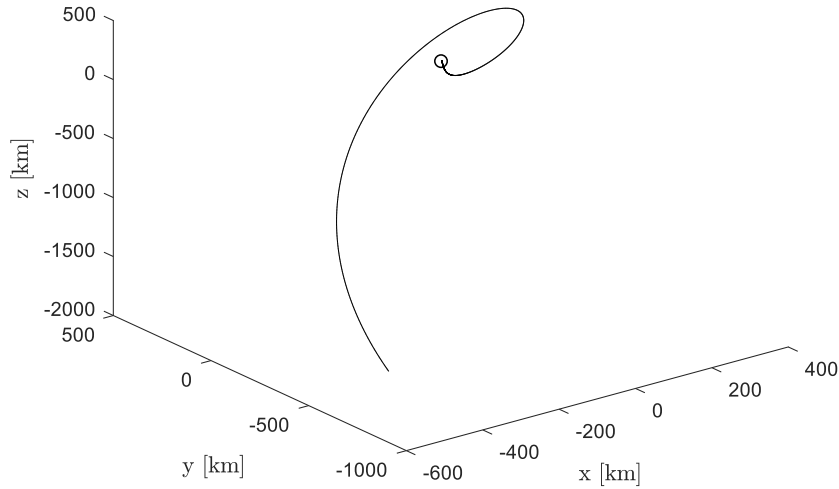


Figure 5. 1-day trajectory of spacecraft with no control about Castalia, simulation 3 (see next section). Open circle indicates the initial state.

Now, consider the case of an LQR controller based on the dynamics of the 2-body problem. This baseline LQR controller uses only 2-body dynamics in the EOMs for its error state – see Equation (16). Therefore, it does not rely on the splitting parameters, only the position and velocity of the spacecraft are used in the controller. Our goal is to show that the adaptive controller outperforms the baseline controller in terms of LQR cost, defined in Equation (17). Thus, in later results, the LQR cost saving is used as a performance metric.

Asteroid Parameters

Three cases are presented in this section. The cases represent scenarios of a spacecraft orbiting an asteroid, each with different physical properties. The three asteroids considered are the contact binaries Castalia, Kleopatra, and 2014 MU₆₉. Table 1 gives the total mass, initial separation distance, mass ratio, and moment of inertia used in the simulation for each asteroid. Since the mass of 2014 MU₆₉ is not known, several masses are used for simulations. 200 kg · m⁻³ is used as a lower bound of the bulk density²⁴. The approximate density of water ice was used next (1000 kg · m⁻³), then three bulk density for different asteroid classes were used⁴⁵. Note that these higher density values are likely inaccurate as a recent study shows that its bulk density may be 500 kg · m⁻³ or less (as low as 280 kg · m⁻³)⁴⁶. Simulations are conducted to gauge the performance of the adaptive controller technique applied to this problem. Note that since the parameter estimates asymptotically converge to their true values (see Appendix B), the performance benefit for the adaptive 3-body controller will be highest over long durations of time. Namely, it is important to determine whether or not the adaptive controller is beneficial in the transient regime (i.e. before the parameters converge to their true values).

Table 1. Asteroid parameter true values used for simulations

Asteroid	$m_{tot} (\rho)$	d_0	μ	I_n
Castalia	1.4192e12 kg	0.860 km	0.3967	0.0765 km ²
2014 MU ₆₉	4.7916e14 kg (200 kg · m ⁻³) 2.3958e15 kg (1000 kg · m ⁻³) 3.3062e15 kg (1380 kg · m ⁻³) 6.4926e15 kg (2710 kg · m ⁻³) 1.2746e16 kg (5320 kg · m ⁻³)	16.9 km	0.4046	30.703 km ²
Kleopatra	4.6369e18 kg	179 km	0.4845	941.60 km ²

All reference trajectories are Keplerian elliptic orbits. The semi-major axis was chosen to be 10 times the initial separation distance. Three different eccentricities were used, one for each asteroid. Initial conditions for each reference trajectory were set at the periapsis of the asteroid system with some initial error offset in both position and velocity. Table 2 gives the values of the semi-major axis, a , and eccentricity, e , for reference orbits used about each asteroid.

Table 2. Reference trajectory conditions used for simulations

Asteroid	a	e
Castalia	8.6 km	0.5
2014 MU ₆₉	168.65 km	0.1
Kleopatra	1790 km	0.25

There are several tunable parameters for the LQR controller: the weights Q , R , F , and N (see Equation (17)). Ultimately, the relative weighting of these parameters is mission dependent. For the simulations conducted here, these

values were chosen to give a realistic level of control for the spacecraft. For all asteroids, $F = 0_{6 \times 6}$ and $N = 0_{6 \times 3}$, and Q is the block matrix:

$$Q = \begin{bmatrix} I_{3 \times 3} & 0_{3 \times 3} \\ 0_{3 \times 3} & 1e4 \cdot I_{3 \times 3} \end{bmatrix} \quad (20)$$

For Castalia and 2014 MU₆₉, $R = 750 \cdot I_{3 \times 3}$ and for Kleopatra $R = 1e4 \cdot I_{3 \times 3}$.

The process noise components for the EKF were selected so that the filter was stable while providing reasonable amounts of variation from the deterministic case. The error covariance matrices can be tuned to suit the problem. Filter stability depends on properly sized covariance matrices. Aside from finding stable values, optimization techniques for tuning the covariance values have been proposed to improve the filter's performance^{47,48,49}, however these techniques usually require extensive computationally expensive Monte Carlo simulations. Process noise covariance values for the (x, y, z) position and $(\dot{x}, \dot{y}, \dot{z})$ velocity for our problem are given in Table 3 as σ_{pos}^2 and σ_{vel}^2 , respectively. For simplicity, the covariance matrix is a diagonal matrix composed of the variance values. Variance for each of the other components of the state X are given in this table, denoted by subscripts. Measurement noise covariance was kept the same for all asteroids: $1e-2 \text{ km}^2$ for the position measurement variance and $1e-10 \text{ km}^2 \text{ s}^{-2}$ for the velocity measurement variance. The measurement time step is taken as 10 seconds for Castalia and 50 seconds for the other two asteroids due to the difference in time scale for the reference trajectories about each asteroid.

Table 3. Kalman filter process noise variance values for the dynamic state used for simulations

Asteroid	σ_{pos}^2 (km^2)	σ_{vel}^2 ($\text{km}^2 \text{ s}^{-2}$)	σ_{d}^2 (km^2)	σ_{d}^2 ($\text{km}^2 \text{ s}^{-2}$)	σ_{θ}^2 (rad^2)	σ_{μ}^2	$\sigma_{L_{n0}}^2$ ($\text{km}^4 \text{ s}^{-2}$)	$\sigma_{I_n}^2$ (km^4)	$\sigma_{\gamma_1}^2$ (rad^2)	$\sigma_{\gamma_2}^2$ (rad^2)
Castalia	1e-10	1e-20	1e-10	1e-20	1e-8	1e-17	1e-19	1e-20	1e-20	1e-20
2014 MU ₆₉	1e-10	1e-20	1e-10	1e-20	1e-8	1e-17	1e-19	1e-14	1e-20	1e-20
Kleopatra	1e-10	1e-20	1e-10	1e-20	1e-8	1e-17	1e-18	1e-10	1e-20	1e-20

For the purpose of simulation, the true asteroid splitting parameters needed to be chosen. While the adaptive controller consistently outperforms the baseline controller (i.e. the controller based on 2-body dynamics only), all of the cases shown in this work have $(\gamma_1, \gamma_2) = (200^\circ, 0^\circ)$. This was used since the adaptive control approach is particularly effective for these angles in the ideal case⁵⁰. This means that without estimation and with perfect knowledge of the asteroid splitting parameters, these angles gave high ideal cost savings using a 3-body controller over the baseline 2-body controller. Intuitively, this scenario places the larger mass closer to the spacecraft for the duration of the simulations causing the performance increase seen. The same angles were then used to determine the cost savings for the more relevant scenario which compares the adaptive 3-body controller to the baseline 2-body controller. To demonstrate the impact of the initial angular momentum on the performance of the proposed controller, values were selected so that the maximum radius of the asteroids' orbit is 30%, 60%, and 90% of the semi-minor axis of the spacecraft's reference orbit in order to avoid a collision. Other parameters are asteroid-dependent and have been addressed in this section, such as the mass ration, μ , and the moment of inertia, I_n .

Adaptive Controller Performance

The stochastic nature of the process noise and estimation noise used during simulation calls for Monte Carlo simulations to gauge the performance of each controller. After 100 simulations were conducted for each different set of splitting parameters, the average cost savings for using the 3-body controller over the 2-body controller was determined. Savings in the adaptive controller's LQR cost (J) over the baseline 2-body controller's cost (J_{baseline}) are tabulated. Table 4, Table 5, and Table 6 show the percent savings for the simulated cases of Castalia, 2014 MU₆₉, and Kleopatra respectively. In each table, L_{n0} is varied to characterize the amount of savings for different splitting

scenarios. Values for L_{n0} are chosen such that for a fixed d_0 , the asteroid systems evolve in Regime II – see Equation (4) – and the maximum radius achieved by either lobe remains smaller than the semi-minor axis of the reference trajectory. Each simulation number corresponds to 100 simulations for each different set of parameters. For 2014 MU₆₉, 50 simulations were conducted for each set of parameters since there are significantly more cases to consider. Tabulated cost savings are average values over the Monte Carlo simulations.

Table 4. Castalia adaptive controller cost savings for various initial angular momentum values.

Simulation No.	L_{n0} (m^2s^{-1})	Results: $\left(1 - \frac{J}{J_{\text{baseline}}}\right) \cdot 100$
1	99.30	3.42%
2	106.1	5.78%
3	111.1	10.4%

Table 5. 2014 MU₆₉ adaptive controller cost savings for various asteroid densities and initial angular momentum values.

Simulation No.	L_{n0} (km^2s^{-1})	ρ ($\text{kg} \cdot \text{m}^{-3}$)	Results: $\left(1 - \frac{J}{J_{\text{baseline}}}\right) \cdot 100$
1	0.0084	200	0.2073%
2	0.0090		0.5684%
3	0.0093		0.7586%
4	0.0189	1000	2.3800%
5	0.0201		2.8993%
6	0.0208		3.5447%
7	0.0222	1380	2.3153%
8	0.0237		4.1396%
9	0.0244		4.2681%
10	0.0311	2710	5.1441%
11	0.0332		6.2447%
12	0.0342		7.4140%
13	0.0435	5320	7.7354%
14	0.0465		11.5296%
15	0.0480		12.8890%

Table 6. Kleopatra adaptive controller cost savings for various initial angular momentum values.

Simulation No.	L_{n0} (km^2s^{-1})	Results: $\left(1 - \frac{J}{J_{\text{baseline}}}\right) \cdot 100$
1	2.358	14.7%
2	2.581	18.9%
3	2.693	20.7%

As Table 4, Table 5, and Table 6 show, the initial angular momentum and the density have a large impact on the performance increase in using the adaptive 3-body controller; the improvement by the proposed method is larger with a higher mass and higher initial angular momentum. A higher initial angular momentum places the asteroids closer to the reference trajectory for the spacecraft to be more affected by the gravity field perturbation driven by the asteroid's separation, making our adaptive controller effective. For a similar reason, a higher asteroid mass also leads to increased performance in the proposed adaptive controller. Specifically, the same orbit (semi-major axis and eccentricity) about higher-density asteroids sees a greater performance increase using the adaptive controller. The proposed adaptive controller has yielded up to a 20.7% savings in cost compared with the traditional 2-body controller. For simulations of 2014 MU₆₉, Figure 6 shows the LQR cost savings as a function of increasing asteroid density for three different splitting scenarios. In the figure, proximity indicates how close the maximum radius of the smaller element gets to the semi-minor axis of the reference trajectory. In this context, closer proximity corresponds to higher initial angular momentum and vice versa. Close, medium, and far correspond to a maximum radius of 90%, 60%, and 30% of the reference trajectory's semi-minor axis, respectively. As the asteroids get closer to the reference trajectory, the separation distance and split parameters become more relevant in the controller, causing the adaptive controller to outperform the baseline controller to a greater extent.

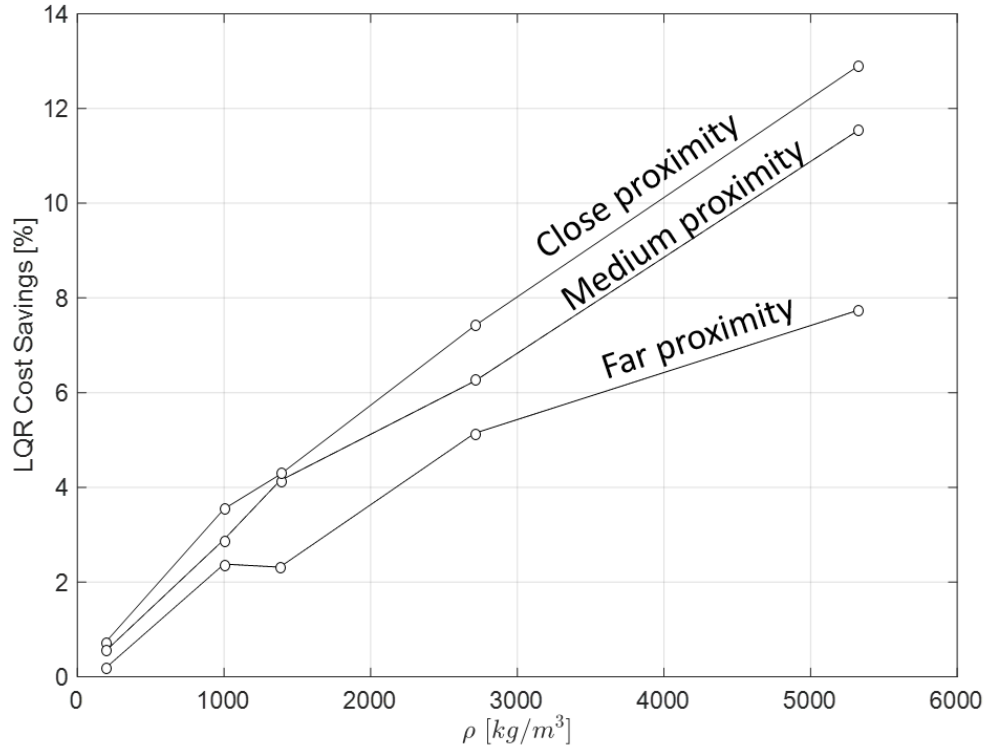


Figure 6. LQR cost savings as a function of asteroid bulk density for the 2014 MU₆₉ case study. Proximity indicates how close the asteroid’s orbit gets to the reference trajectory of the spacecraft.

Estimation of both dynamic and constant components of the state X is critical for the adaptive controller to function properly. Each parameter converges to its true value. For a single simulation about the asteroid Castalia, the asteroid splitting parameter estimates are plotted in Appendix B.

To illustrate the controller’s performance, the trajectory of the spacecraft about Castalia is plotted for one reference trajectory orbital period using the adaptive controller. Since the system is observable, the unknown parameters will converge with or without the control scheme discussed before. The control, however, will only drive the trajectory error to zero if the state and parameter estimates are close. Since the type of controller depends on the error that is relatively small (it was derived via linearization about zero error), if the error becomes too large before the unknown parameters are estimated well, then there is no guarantee that the control objective will be met. For all of the cases considered here, the estimates converge to values fast enough such that the controller drives the position error and velocity error to zero. Figure 7 shows the trajectory using the adaptive controller for two cases: one with a higher cost for large control usage (left) and one with a high cost for large trajectory error (right).

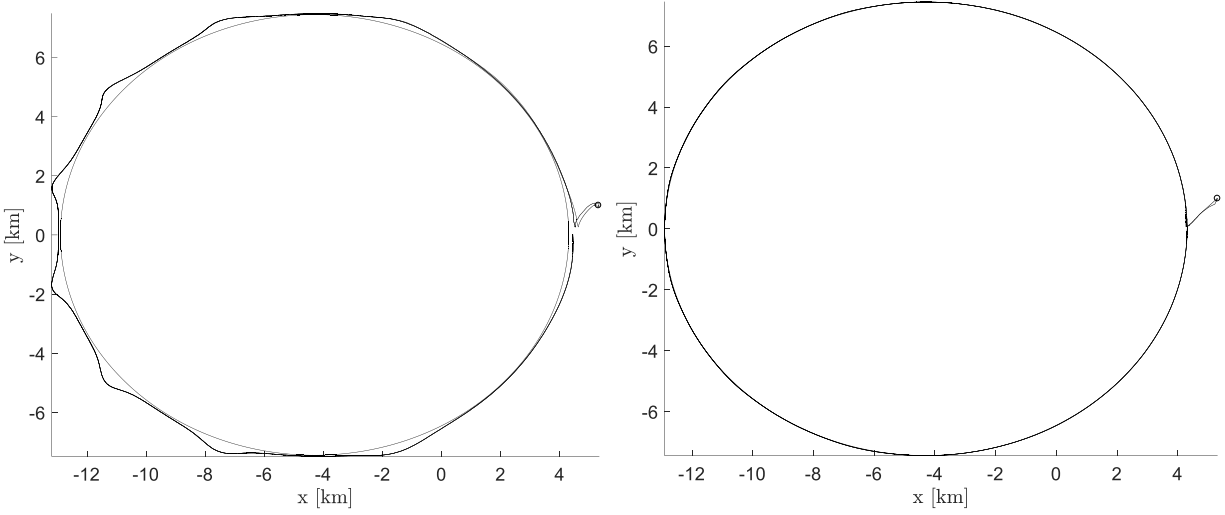


Figure 7. 1-orbit trajectory about Castalia. The left figure uses a higher cost for control in the LQR controller. The right figure uses a high cost for state error in the LQR controller.

CONCLUSION

The problem of controlling a spacecraft's trajectory in the vicinity of a separating contact-binary asteroid system with unknown features was studied. The proposed method separates the estimation and control design into two parts via the Certainty Equivalence Principle (CEP). State and parameter estimates are provided using a continuous-discrete Extended Kalman Filter (EKF). Then using the 3-body problem model and current parameter and state estimates, the Linear Quadratic Regulator (LQR) controller solves a local, quadratic minimization problem to determine the input for each time step. The indirect adaptive control scheme proposed has yielded promising results; it has simultaneously estimated the unknown asteroid system parameters and stabilized the spacecraft's trajectory error. For larger, denser asteroids, simulations have shown up to a 20% improvement in performance while using the adaptive controller over the baseline 2-body controller.

This work has multiple potential directions for extensions. Direct adaptive controllers based on Lyapunov control design would add robustness to the controller in combination with Sontag's universal formula^{51,52}. Improved asteroid models and observations can be added to lend more fidelity to the method and to capture more realistic information about the separating contact-binary system. Specifically, the model can be improved by using more representative gravity models for asteroids and adding external perturbations such as solar radiation pressure.

NOTATION

Symbols Used

d, \dot{d}, \ddot{d}	Separation distance, velocity, and acceleration, respectively, between two asteroid lobes.
d_0	Initial separation distance between asteroid lobes.
$\Omega, \dot{\Omega}$	Angular velocity and acceleration, respectively, of the asteroids' rotating frame.
Ω_0	Initial angular velocity of asteroids' rotating frame.
m_1, m_2, m_{tot}	Mass of first asteroid lobe, second asteroid lobe, then the total mass ($m_1 + m_2$), respectively.
$(x, y, z), (\dot{x}, \dot{y}, \dot{z}), (\ddot{x}, \ddot{y}, \ddot{z})$	Cartesian spacecraft position, velocity, and acceleration components, respectively.

μ	Mass ratio parameter between the two lobes: m_2/m_{tot} .
G	Gravitation constant. In S.I. units: $6.67408\text{e-}11 \text{ m}^3\text{kg}^{-1}\text{s}^{-2}$.
γ_1, γ_2	First two Euler angles in the XYZ sequence relating the inertial and asteroids' rotating frames.
θ	Last Euler angle in the XYZ sequence. Integral of the angular rate Ω .
I_n	Summed moment of inertia about the center of mass of each asteroid lobe, divided by m_{tot} .
L_{n0}	Initial angular momentum of the asteroid system.
E_{tot}	Total energy of the binary asteroid system (kinetic and gravitational potential energy).
X, X_d	Extended state used for Kalman filter estimation and desired state (reference trajectory).
J, J_{baseline}	LQR cost using the 3-body adaptive controller and the 2-body baseline controller, respectively.
n, m	Number of components in the state and in the control, respectively
ϕ_i	i^{th} successive Lie derivative used for nonlinear observability check.
Φ	Concatenated vector of successive Lie derivatives $\phi_i \ i \in \{0, 1, 2, \dots, n-1\}$.
u	Control input vector.
$\sigma_{\text{parameter}}^2$	The variance of a parameter used for either process or measurement noise in the EKF.
ξ, f_ξ, h_ξ	Dummy state variable, vector field, and observation mapping for observability analysis.
$\bar{\xi}, \bar{\xi}^-, P_{EKF}, P_{EKF}^-$	Estimated state, predicted estimated state, error matrix, and predicted error matrix for the EKF.
$\tau, \Delta t$	Current time and measurement time step used for Kalman filter update and prediction steps.
W, Q_{EKF}, V, R_{EKF}	Process noise RV, its covariance matrix, Measurement noise RV, and its covariance matrix.
e, f_e, g_e	Error state and error dynamics vector fields and used for LQR stabilization.
A_e, B_e	Matrices used for linear error dynamics in LQR framework.
Q, R, F, N	Weight matrix for the state, control, final state, and state-control cross coupling in LQR cost.
P, K	Solution to the Algebraic or Differential Ricatti Equation. Used to find LQR control gain K .
a, e	Semi-major axis and eccentricity of Keplerian elliptic reference trajectory.
$I_{i \times i}, 0_{i \times j}$	i by i identity matrix and i by j matrix of zeros, respectively.

Acronyms Used

CAESAR	Comet Astrobiology Exploration SAmples Return
CEP	Certainty Equivalence Principle
CLF	Control Lyapunov Function

DART	Double Asteroid Redirect Test
DRE	Differential Ricatti Equation
EKF	Extended Kalman Filter
EOM	Equation of Motion
JAXA	Japanese Aerospace Exploration Agency
LQR	Linear Quadratic Regulator
NASA	National Aeronautics and Space Administration
NEA	Near Earth Asteroid
ODE	Ordinary Differential Equation
OSIRIS-Rex	Origins Spectral Interpretation Resource Identification Security-Regolith Explorer
RV	Random Vector
SRP	Solar Radiation Pressure
UIUC	University of Illinois at Urbana-Champaign
UKF	Unscented Kalman Filter

APPENDIX A: DERIVATIONS OF THE CONDITIONS

Conservation of energy is used to prove the conditions in Equation (4). The total energy of the system at a separation distance d is the sum of the rotational, kinetic, and potential energy of the asteroid lobes, given here as Equation (21):

$$E_{tot}(d) = \underbrace{\frac{1}{2}m_{tot}\Omega_0^2 \cdot \frac{(I_n + \mu(1-\mu)d_0^2)^2}{I_n + \mu(1-\mu)d^2} + \frac{1}{2}m_{tot}\mu(1-\mu)\dot{d}^2}_{\text{Kinetic (Rotational and Translational)}} - \underbrace{\frac{Gm_{tot}^2\mu(1-\mu)}{d}}_{\text{Potential}} \quad (21)$$

The velocity in the kinetic term can be solved for using conservation of energy, using the energy of the known, initial offset d_0 . The energy balance is given below, assuming that the two lobes are initially at rest with respect to each other:

$$E_{tot}(d) = E_{tot}(d_0) = \underbrace{\frac{1}{2}m_{tot}\Omega_0^2(I_n + \mu(1-\mu)d_0^2)}_{\text{Kinetic}} - \underbrace{\frac{Gm_{tot}^2\mu(1-\mu)}{d_0}}_{\text{Potential}} \quad (22)$$

First, consider the condition that differentiates Case II and Case III. If the kinetic energy portion of the total energy is greater than the potential energy, then the conditions for Case III are recovered. Thus, that condition can be derived from Equation (22).

Next, consider the condition that differentiates Case II and Case I. If the two lobes are still connected as in Case I, then their separation distance is constrained to be d_0 . The upper bound for this case is given by the conditions (Ω_0, d_0) where the gravitational force is exactly equal to the centrifugal force. Setting $\ddot{d} = 0$ in Equation (1) and evaluating the expression at the initial time for the angular velocity, the following condition is derived:

$$\Omega_0 = \sqrt{\frac{Gm_{tot}}{d_0^3}} \quad (23)$$

If the gravitational force exceeds the centrifugal force, but the system does not have sufficient kinetic energy to overcome the gravitational potential, then the system is in Case II. For a given d_0 , feasible angular velocities for this regime are bounded below by Equation (23) and above by the angular velocity given by setting $E_{tot} = 0$ in Equation (22) and solving for Ω_0 .

There are asteroids which cannot evolve in Case II and can only stay together or reach escape after splitting. This occurs when the condition given below is met.

$$\frac{Gm_{tot}}{d_0^3} \geq \frac{Gm_{tot}}{d_0} \cdot \frac{2\mu(1-\mu)}{I_n + \mu(1-\mu)d_0^2} \quad (24)$$

This means that the condition on the angular velocity for separation is greater than or equal to the condition for escape. Since $d_0 > 0$, $I_n > 0$, and $\mu(1-\mu) > 0$, a simpler expression for asteroids in this category is given as follows:

$$I_n \geq \mu(1-\mu)d_0^2 \quad (25)$$

APPENDIX B: ESTIMATION RESULTS

This section contains the parameter estimation results of a single simulation about the asteroid Castalia. Each parameter is plotted until convergence to the true values occurs (roughly the first 5 hours). In all plots, the dotted lines represent the true value and the solid line represents the estimated value. Each parameter is initialized arbitrarily, without using the unknown, true values.

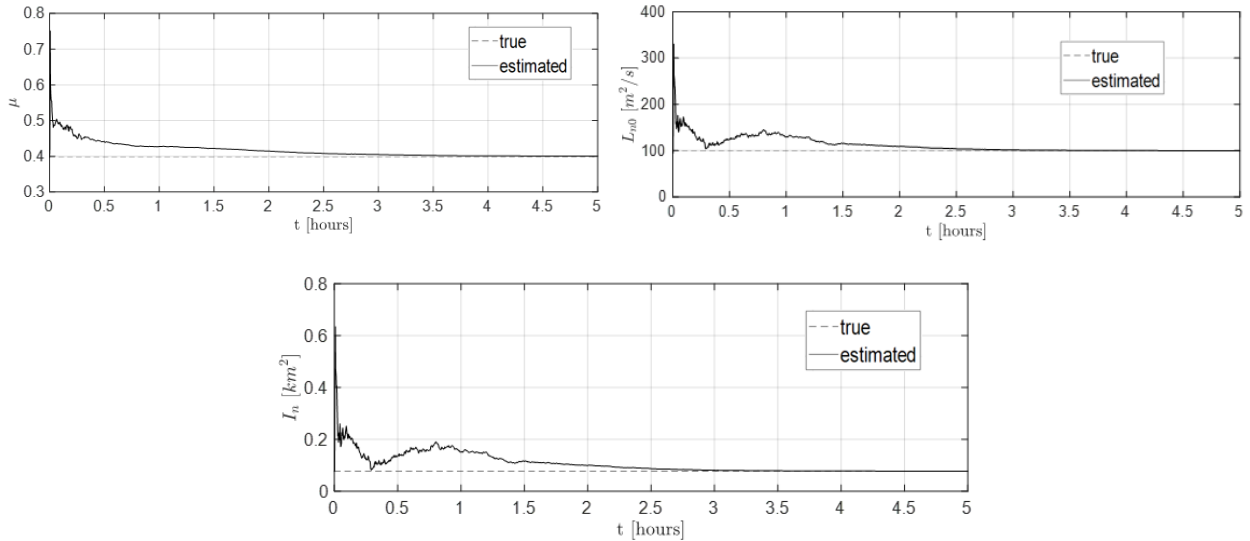


Figure 8. Parameter estimation for μ (top left), L_{n0} (top right), and I_n (bottom) for Castalia simulation 1.

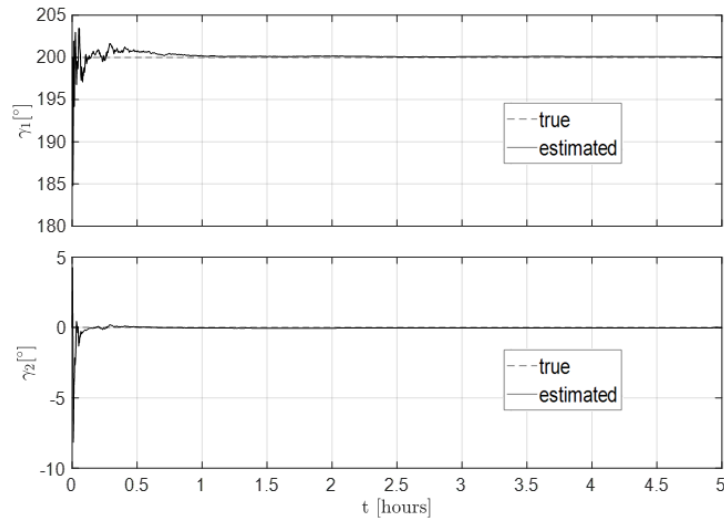


Figure 9. Parameter estimation for γ_1 (top) and γ_2 (bottom) for Castalia simulation 1

REFERENCES

- ¹ A. Fujiwara, et al., "The Rubble-Pile Asteroid Itokawa as Observed by Hayabusa," *Science*, vol. 312, pp. 1330-1334, 2006.
- ² M. Yoshikawa, J. Kawaguchi, A. Fujiwara, A. Tsuchiyama, "Hayabusa Sample Return Mission," In *Asteroids IV* (P. Michel et al. eds), pp. 397-418, 2015.
- ³ S. Watanabe, et al., "Hayabusa2 Arrives at the Carbonaceous Asteroid 162173 Ryugu – A Spinning Top – Shaped Rubble Pile," *Science*, vol. 364, no. 6437, pp. 268-272, 2019.
- ⁴ K. Kitazato, et al., "The Surface Composition of Asteroid 162173 Ryugu from hayabusa2 Near-Infrared Spectroscopy," *Science*, vol. 364, no. 6437, pp. 272-275, 2019.
- ⁵ S. Sugita, et al., "The Geomorphology, Color, and Thermal Properties of Ryugu: Implications for planet-Body Processes," *Science*, vol. 364, no. 6437, 2019.
- ⁶ D. S. Lauretta, et al., "The OSIRIS-REx target asteroid (101955) Bennu: Constraints on its physical, geological, and dynamical nature from astronomical observations," *Meteoritics & Planetary Science*, vol. 50, pp. 834-849, 2014.
- ⁷ D. S. Lauretta, et al., "OSIRIS-REx: Sample Return from Asteroid (101955) Bennu," *Space Science Reviews*, vol. 212, no. 1, pp. 925-984, 2017.
- ⁸ D. D. Mazanek, R. G. Merrill, J. R. Brophy and R. P. Mueller, "Asteroid Redirect Mission concept: A bold approach for utilizing space resources," *Acta Astronautica*, vol. 117, pp. 163-171, 2015.
- ⁹ R. C. Anderson, D. J. Scheres and S. Chesley, "Binary Asteroid In-Situ Explorer Mission (BASiX): A Mission Concept to Explore a Binary Near Earth Asteroid System," in *45th Lunar and Planetary Science Conference*, Woodlands, Texas, 2014.
- ¹⁰ M. Elvis, "Let's mine asteroids—for science and profit: the commercial dream of trawling space for valuable minerals could bring enormous benefits to a wide range of sciences," *Nature*, vol. 485, no. 7400, p. 549, 2012.
- ¹¹ P. Monahan, "Space mining gets a boost from tiny Luxembourg," *Science*, 2016.
- ¹² A. F. Cheng, et al., "AIDA DART asteroid deflection test: Planetary defense and science objectives," *Planetary and Space Science*, vol. 157, pp. 104-115, 2018.
- ¹³ M. Hirabayashi, et al., "Constraints on the perturbed mutual motion in Didymos due to impact-induced deformation of its primary after the DART impact," *The Astrophysical Journal Letters*, vol. , pp. , 2017.
- ¹⁴ M. Hirabayashi, et al., "Assessing possible mutual orbit period change by shape deformation of Didymos after a kinetic impact in the NASA-led Double Asteroid Redirection Test," *Advances in Space Research*, vol. 63, pp. 2515-2534, 2019.

-
- ¹⁵ B. Rozitis, E. MacLennan and J. P. Emery, "Cohesive forces prevent the rotational breakup of," *Nature*, vol. 512, pp. 174-176, 2014.
- ¹⁶ M. Hirabayashi and D. J. Scheeres, "Stress and failure analysis of rapidly rotating asteroid (29075) 1950 DA," *The Astrophysical Journal Letters*, vol. 798, pp. 1-5, 2015.
- ¹⁷ L. A. M. Benner, M. W. Busch, J. D. Giorgini, P. A. Taylor and J.-L. Margot, "Radar Observations of Near-Earth and Main-Belt Asteroids," in *Asteroids IV*, Tuscon, University of Arizona Press, 2015, pp. 165-182.
- ¹⁸ D. Jewitt, J. Agarwal, J. Li, H. Weaver, M. Mutchler and S. Larson, "Disintegrating Asteroid P/2013 R3," *The Astrophysical Journal Letters*, vol. 784, 2014.
- ¹⁹ M. K. Shepard, B. Timerson, D. J. Scheeres, L. A. M. Benner, J.D. Giorgini, E. S. Howell, C. Magri, M. C. Nolan, A. Springmann, P. A. Taylor, and A. Virkki, "A Revised Shape Model of Asteroid (216) Kleopatra," in *Icarus*, vol. 311,, pp. 197-209, 2019.
- ²⁰ R. S. Hudson and S. J. Ostro, "Shape of Asteroid 4769 Castalia (1989 PB) from Inversion of Radar Images," *Science*, vol. 263, no. 5149, pp. 940-943, 1994.
- ²¹ T. Talbert, "New Horizons Spacecraft Returns Its Sharpest Views of Ultima Thule," NASA, 2019.
- ²² Hu, S., J. Ji, D. C. Richardson, Y. Zhao and Y. Zhang, "The formation mechanism of 4179 Toutatis' elongated bi-lobed," *Monthly Notices of the Royal Astronomical Society*, vol. 478. , 2018.
- ²³ W. R. Johnston, "Contact Binary Asteroids, TNOs, and Comets," 7 July 2018. [Online]. Available: <http://www.johnstonsarchive.net/astro/contactbinast.html>.
- ²⁴ C. J. Bierson, O. Umurhan , R. A. Beyer, T. R. Lauer, M. W. Buie1, A. H. Parker, M. Kinczyk, K. Runyon, W. M. Grundy, J.J. Kavelaars, A. M. Zangari, M. R. El-Maarry, D. T. Britt, J. M. Moore, A. Verbiscer, J. W. Parker, C. B. Olkin, H. A. Weaver, J. R. Spencer, S. A. Stern, and the New Horizons Geology, Geophysics, and Imaging (GGI) Team, "A CONTACT BINARY IN THE KUIPER BELT: THE SHAPE AND POLE OF (486958) 2014 MU69," in *50th Lunar and Planetary Science Conference*, Woodlands, Texas, 2019.
- ²⁵ M. Hirabayashi, D. J. Scheeres, S. R. Chesley, S. Marchi, J. W. McMahon, J. Steckloff, S. Mottola, S. P. Naidu, and T. Bowling., "Fission and Reconfiguration of Bilobate Comets as Revealed by 67P/Churyumov-Gerasimenko," *Nature*, vol. 534, pp. 352-355, 2016.
- ²⁶ E. Herrera-Sucarrat, P. L. Palmer, and R. M. Robert, "Modeling the Gravitational Potential of a Nonspherical Asteroid," *Journal of Guidance, Control, and Dynamics*, vol. 36, no. 3, 2013.
- ²⁷ G. Romain and B. Jean-Pierre, "Ellipsoidal Harmonic Expansions of the Gravitational Potential: Theory and Application," in *Celestial Mechanics and Dynamical Astronomy*, vol. 79, pp. 235-275, 2001.
- ²⁸ R. A. Werner and D. J. Scheeres, "Exterior gravitation of a polyhedron derived and compared with harmonic and mascon gravitation representations of asteroid 4769 Castalia." *Celestial Mechanics and Dynamical Astronomy*, 65:314-344, 1997.
- ²⁹ D. J. Scheeres and P. Sánchez, "Implications of Cohesive Strengths in Asteroid Interiors and Surfaces and its Measurement", in *Progress in Earth and Planetary Science*, 5:25, 2018.
- ³⁰ D. C. Richardson, O. S. Barnouin, L. A. M. Benner, W. F. Bottke Jr., A. Campo Bagatin, A. F. Cheng, M. Hirabayashi, C. Maurel, J. W. McMahon, P. Michel, N. Murdoch, S. P. Naidu, P. Pravec, A. S. Rivkin, D. J. Scheeres, P. Scheirich, K. Tsiganis, Y. Zhang, and the AIDA Dynamical and Physical Properties of Didymos Working Group, "Dynamical and Physical Properties of 65803 Didymos, the Proposed AIDA Mission Target," AAS/Division for Planetary Sciences Meeting Abstracts 48, AAS/Division for Planetary Sciences Meeting Abstracts, Vol. 48, 2016, p. 123.17.
- ³¹ Y. Takahashi, "Gravity Field Characterization around Small Bodies," University of Colorado Department of Aerospace, Boulder, 2013.
- ³² G. Romain and B. Jean-Pierre, "Ellipsoidal Harmonic Expansions of the Gravitational Potential: Theory and Application," in *Celestial Mechanics and Dynamical Astronomy*, vol. 79, pp. 235-275, 2001.
- ³³ R. A. Werner and D. J. Scheeres, "Exterior gravitation of a polyhedron derived and compared with harmonic and mascon gravitation representations of asteroid 4769 Castalia." *Celestial Mechanics and Dynamical Astronomy*, 65:314-344, 1997.
- ³⁴ I. D. Landau, R. Lozano, M. M'Saad and A. Karimi, "Introduction to Adaptive Control," in *Adaptive Control: Alorithms, Analysis and Applications*, Springer, 2011, pp. 1-33.
- ³⁵ L. Ljung, "Asymptotic Behavior of the Extended Kalman Filter as a Parameter Estimator for Linear Systems," *IEEE Transactions on Automatic Control*, Vols. AC-24, no. 1, pp. 36-50, 1979.
- ³⁶ D. Del Vecchio and R. M. Murray, "Observability and Local Observer Construction for Unknown Parameters in Linearly and Nonlinearly Parameterized Systems," in *American Control Conference*, Denver, 2003.

-
- ³⁷ X. Sun, L. Jin and M. Xiong, "Extended Kalman Filter for Estimation of Parameters in Nonlinear State-Space Models of Biochemical Networks," *PLoS ONE*, vol. 3, no. 11, pp. 1-13, 2008.
- ³⁸ R. Hermann and A. J. Krener, "Nonlinear Controllability and Observability," *IEEE Transactions on Automatic Control*, Vols. AC-22, no. 5, pp. 728-740, 1977.
- ³⁹ D. Simon, "Optimal State Estimation: Kalman, H [infinity] and Nonlinear Approaches," John Wiley and Sons, 2006.
- ⁴⁰ S. J. Julier and J. K. Uhlmann, "Unscented Filtering and Nonlinear Estimation," in *IEEE*, 2004.
- ⁴¹ A. J. Krener and K. Ide, "Measures of Unobservability," in *IEEE Conference on Decision and Control and Chinese Control Conference*, Shanghai, 2009.
- ⁴² J. E. Prussing and B. A. Conway, *Orbital Mechanics*, Second Edition, New York: Oxford University Press, 1993.
- ⁴³ R. M. Murray, Class Lecture, Topic: "Lecture 2 - LQR Control," Control and Dynamical Systems, California Institute of Technology, Pasadena, pp. 3-4, 2006.
- ⁴⁴ R. Suarez, J. Alvarez-Ramirez and J. Solis-Daun, "Linear Systems with Bounded Inputs: Global Stabilization with Eigenvalue Placement," *International Journal of Robust and Nonlinear Control*, vol. 7, pp. 835-845, 1997.
- ⁴⁵ G. A. Krasinsky, E. V. Pitjeva, M. V. Vasilyev and E. I. Yagudina, "Hidden Mass in the Asteroid Belt," *Icarus*, vol. 158, pp. 98-105, 2002.
- ⁴⁶ S. A. Stern et al., "Initial results from the New Horizons Exploration of 2014 MU₆₉, a Small Kuiper Belt Object," *Science*, vol. 364, 2019.
- ⁴⁷ N. Kaur, A. Kaur, "Tuning of Extended Kalman Filter for Nonlinear State Estimation," *IOSR Journal of Computer Engineering (IOSR-JCE)*, vol. 18, no. 5, pp. 14-19, 2016.
- ⁴⁸ T. D. Powell, "Automated Tuning of an Extended Kalman Filter Using the Downhill Simplex Algorithm," *Journal of Guidance, Control, and Dynamics*, vol. 25, pp. 901-908, 2002.
- ⁴⁹ N. Kaur, A. Kaur, "A Review on Tuning of Extended Kalman Filter Using Optimization Techniques for State Estimation," *International Journal of Computer Applications*, vol. 145, no. 15, 2016.
- ⁵⁰ T. M. Silva, "Spacecraft Trajectory Tracking and Parameter Estimation in the Presence of a Splitting Contact Binary Asteroid", University of Illinois at Urbana-Champaign Department of Aerospace Engineering, Urbana, 2019.
- ⁵¹ E. D. Sontag, "A 'Universal' Construction of Artstein's Theorem on Nonlinear Stabilization," *Systems & Control Letters*, vol. 13, pp. 117-123, 1989.
- ⁵² Y. Lin and E. D. Sontag, "A Universal Formula for Stabilization with Bounded Controls," *Systems & Control Letters*, vol. 16, pp. 393-397, 1991.